NASA Technical Memorandum 4576

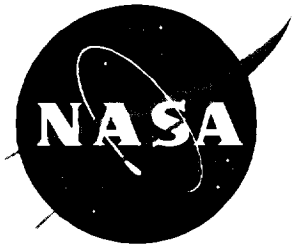

Planar Rayleigh Scattering and Laser-Induced Fluorescence for Visualization of a Hot, Mach 2 Annular Air Jet

R. Jeffrey Balla
Langley Research Center • Hampton, Virginia

National Aeronautics and Space Administration
Langley Research Center • Hampton, Virginia 23681-0001

October 1994

The use of trademarks or names of manufacturers in this report is for accurate reporting and does not constitute an official endorsement, either expressed or implied, of such products or manufacturers by the National Aeronautics and Space Administration.

Acknowledgments

The author appreciated the contributions of the following Langley staff members: B. Shirinzadeh, M. E. Hillard, R. J. Exton, G. B. Northam, O. Jarrett, R. Gregory, B. Barnes, W. Simmons, and R. R. Antcliff.

This publication is available from the following sources:

NASA Center for AeroSpace Information
800 Elkridge Landing Road
Linthicum Heights, MD 21090-2934
(301) 621-0390

National Technical Information Service (NTIS)
5285 Port Royal Road
Springfield, VA 22161-2171
(703) 487-4650

Introduction

Instantaneous and average experimental information in supersonic and hypersonic flow fields can be quite useful when compared with computational fluid dynamic (CFD) calculations. (See ref. 1.) Quantitative temperature measurements can be made and qualitative information can be obtained from flow-field visualization studies. Qualitative information may include the location of flow constituents, the size and location of both instantaneous and average flow structures, and the unsteadiness of the flow field. Traditional methods of measurement are intrusive; that is, they rely on the insertion of probes into the flow field. However, such methods can affect the parameters they seek to measure. (See refs. 2 and 3.) With the introduction of high-power laser systems into research applications, optical diagnostic techniques can now be applied to measure desired parameters. Optical techniques have several advantages over probes: they are nonintrusive, instantaneous, and capable of measuring parameters in two dimensions over the flow field.

Two successful optical techniques for unseeded supersonic, hypersonic, and combusting flows are Rayleigh scattering (refs. 4–9) and laser-induced fluorescence. (See refs. 10–16.) Rayleigh scattering generates a signal related to the sum of the mole fraction, weighted Rayleigh cross sections for each species in the flow field. Under certain conditions, this signal can be related to temperature. Laser-induced fluorescence generates a signal which can be related to the density of the individual species being probed. In many cases, the hydroxyl radical (OH) is probed because it is an intermediate in the combustion process and is easily accessible spectroscopically with current laser technology.

This study has three objectives: to demonstrate the advantage of a xenon chloride (XeCl) tunable laser on both techniques for the successful generation of planar information in the vitiated air component of an unseeded Mach 2 flow field, to investigate the potential of planar Rayleigh scattering (PRS) to obtain planar temperature data in the vitiated air component, and to use planar laser-induced fluorescence (PLIF) to obtain qualitative information about the location and the instantaneous and average flow structures that contain OH.

Symbols

C	correction factor (eq. (5))
cm^{-1}	wave numbers
$d\sigma/d\Omega$	differential Rayleigh cross section
$(d\sigma/d\Omega)_{\mathrm{eff}}$	effective differential Rayleigh cross section
H_2	hydrogen molecule
H_2O	water molecule
k	universal gas constant divided by Avogadro's number
N	molecular number density
N_t	sum of molecular number densities of each component in flow
N_2	nitrogen molecule
O	oxygen atom
OH	hydroxyl molecule
O_2	oxygen molecule
P	pressure, atm
Q1(3), P1(1)	spectroscopic notation used to describe transition probed in OH molecule
R	universal gas constant
S	signal level with units of photoelectrons per laser pulse
T	temperature, K
V	excitation volume
X, Y, Z	Cartesian coordinates
XeCl	xenon chloride
$X(i)$	mole fraction of species i
$\Delta n/n$	fractional population of OH molecules in rotational level from which excitation originates
$\Delta\nu_{\mathrm{eff}}$	effective absorption line width for OH transition
η_{eff}	excited molecules fraction which emits photon; fluorescence quantum yield
η_{PMT}	photocathode quantum efficiency
η_t	transmission of collection optics
ν	radiation frequency, cm^{-1}
σ_{o}	integrated absorption cross section
Φ	laser photon flux
Ω	solid angle of collection

Abbreviations:

BS1–BS3	beam splitters

CCD	charge-coupled device; video camera array detector
CFD	computational fluid dynamics
CL1–CL4	cylindrical lenses 1 through 4; laser sheet-forming optics
FWHM	full width at half maximum of OH transition line width; laser line width
HR1	high reflector
LIF	laser-induced fluorescence
L1–L6	spherical lens
PD1, PD2	sample-and-hold photodiode detectors
PLIF	planar laser-induced fluorescence
PMT	photomultiplier tube
PRS	planar Rayleigh scattering
rms	root mean square

Principle of Laser Diagnostic Technique

Rayleigh Scattering

Rayleigh scattering is the result of elastic scattering of light from molecules. This process generates radiation with no change in frequency. The Rayleigh signal, which can be expressed as the number of photoelectrons per laser pulse (ref. 5), is given by

$$S = N\frac{d\sigma}{d\Omega}\Phi V\Omega\eta_t\eta_{\mathrm{PMT}} \qquad (1)$$

where N is the number density of molecules, $d\sigma/d\Omega$ is the differential Rayleigh cross section, Φ is the laser photon flux, V is the excitation volume, Ω is the solid angle of collection, η_t is the transmission of collection optics, and η_{PMT} is the photocathode quantum efficiency.

The flow field that exits the outer injector at a Mach number of 2 comprises several species which collectively are known as vitiated air. Vitiated air is formed from the combustion of hydrogen and air in the settling chamber; oxygen is then added to replace that consumed in combustion. The resulting vitiated air is hot and has an oxygen content of 21 percent. The major vitiated air components in this portion of the flow field are molecular nitrogen (N_2), molecular oxygen (O_2), and water (H_2O) (refs. 17 and 18) in the proportions shown in tables I and II. Cheng et al. (ref. 19) and Cheng, Wehrmeyer, and Pitz (ref. 20) measured average mole fractions of these three components in amounts similar to those tabulated. Cheng et al. (ref. 19) and Cheng, Wehrmeyer, and Pitz (ref. 20) also measured the average mole fractions of hydrogen in the vitiated air. They reported a value less than 0.0001, which indicates it was a minor species. Based on equation (1), the molecular Rayleigh signal in this flow field will be related to the sum of the densities of the components of vitiated air, weighted by the individual cross sections.

Table I. Nominal Conditions for Supersonic Burner

General parameters:	
Air mass flow rate (±2 percent), kg/sec	0.0735
H_2 mass flow rate (±2 percent), kg/sec	0.00173
O_2 mass flow rate (±3 percent), kg/sec	0.0211
Fuel mass flow rate (±3 percent), kg/sec	0.000362
Nozzle exit inside diameter, mm	17.78
Fuel injector inside diameter, mm	2.36
Fuel injector outside diameter, mm	3.81
Fuel injector height above outer nozzle, mm	2.8
Stagnation conditions:	
Pressure (±4), torr	5930
Temperature, K	1752
Vitiated air exit conditions:	
Pressure, torr	760
Temperature, K	1250
Mach number	2
Velocity, m/sec	1417
O_2 mole fraction	0.201
N_2 mole fraction	0.544
H_2O mole fraction	0.255
Fuel exit conditions:	
Pressure, torr	796
Temperature, K	545
Mach number	1
Velocity, m/sec	1780
H_2 mole fraction	1

Table II. Mole Fractions of Relevant Supersonic Burner Constituents

Condition	Mole fraction for—			
	N_2	O_2	H_2O	OH
Room air	0.79	0.21	0	
Vitiated air	.544	.201	.255	<0.0001
Combusted, vitiated air	.495	.091	.414	

This flow field has two characteristics that permit the signal obtained in the Rayleigh experiments to be converted to a temperature map. First, the pressure

throughout this flow field was 760 torr and assumed uniform. (See the section, "Supersonic Burner.") Second, the flow field comprised three major species which possess similar Rayleigh cross sections at the wavelengths shown in table III.

Table III. Differential Rayleigh Cross Sections of Relevant Species as Function of Wavelength

[Cross sections calculated from refractive index data in reference 22; values multiplied by 1×10^{28}; units in cm^2/sr]

Wavelength, nm	Rayleigh cross section for			
	N_2	O_2	H_2O	OH
514.5	7.03	5.78	5.01	10.86
363.8	29.28	24.44	21.43	57.88
308.0	58.90	49.73	44.03	146.00

Apparently, no Rayleigh cross-section measurements are available at 308 nm for the three major species. Shardanand and Prasad Rao (ref. 21) have measured the frequency dependence of the Rayleigh cross sections for several gases, including O_2 and N_2. They have shown that the values of the Rayleigh cross sections can be calculated from the molecule index of refraction and can be extrapolated from one wavelength to another using a radiation frequency ν^4 dependence. Their data were acquired from 694.3 to 363.8 nm but suggest that extrapolation over a wider range is possible. Unfortunately, their measurements did not include water. Gardiner, Hidaka, and Tanzawa (ref. 22) present recommended values for calculating the wavelength dependence of the refractive index for many important combustion species. Their data were used to calculate all the Rayleigh cross sections in table III, which agree with the results of Shardanand and Prasad Rao. (See ref. 21.)

The effective differential Rayleigh cross section $(d\sigma/d\Omega)_{\text{eff}}$ of a gas mixture is the sum of the mole fraction $X(i)$ weighted cross sections $[d\sigma(i)/d\Omega]$ and can be expressed (refs. 5 and 6) as

$$\left(\frac{d\sigma}{d\Omega}\right)_{\text{eff}} = X(\text{N}_2)\left[\frac{d\sigma(\text{N}_2)}{d\Omega}\right] + X(\text{O}_2)\left[\frac{d\sigma(\text{O}_2)}{d\Omega}\right] + X(\text{H}_2\text{O})\left[\frac{d\sigma(\text{H}_2\text{O})}{d\Omega}\right] \tag{2}$$

Therefore, equation (1) can be written as

$$S = N_t\left(\frac{d\sigma}{d\Omega}\right)_{\text{eff}} \Phi V \Omega \eta_t \eta_{\text{PMT}} \tag{3}$$

where N_t represents the sum of the number densities of each component in the flow. Consider the value of the effective differential Rayleigh cross section for room air, vitiated air, and combusted vitiated air (defined in the next paragraph) based on the mole fractions and differential Rayleigh cross sections of the constituent species in tables II and III. The respective values at 308 nm are 56.97×10^{-28}, 53.26×10^{-28}, and 51.91×10^{-28} cm^2/sr. If the effective cross section for vitiated air is chosen as the reference point, the large changes in mole fraction for the other cases result in only a -2.5-percent deviation of the effective cross section for combusted vitiated air and a 7.0-percent deviation for room air. Therefore, if the flow field contained mainly N_2, O_2, and H_2O and possessed the expected Rayleigh cross sections, then the effective Rayleigh cross section can be considered independent of flow-field composition. In these experiments, the calibration is based on the effective Rayleigh cross section for room air.

Combusted vitiated air occurs when the oxygen has reacted fully with sufficient hydrogen to produce water. This composition will be a downstream element when all the hydrogen from the center injector is combusted.

The relationship between pressure P, density N, and temperature T is expressed by the ideal gas equation

$$P = NkT \tag{4}$$

Equation (3) shows that the Rayleigh signal is related to the total number density. Substitution of equation (4) into equation (3) shows that the Rayleigh signal is inversely related to the temperature. (See refs. 5 and 6.) The supersonic burner was operated to produce a vitiated air flow field in which the static pressure was assumed uniform at 760 torr; the calibration data were acquired under a known temperature (296 K). Normalization of the Rayleigh signal produced the following relation:

$$T_2 = T_1 \frac{S_1}{S_2 C} \tag{5}$$

where S_1 in this experiment is the signal generated by atmospheric-pressure air at room temperature (T_1), S_2 is the signal generated by the vitiated flow at temperature T_2, and C is a factor equal to 1.07 to correct for the difference in the effective Rayleigh cross section between the room-air calibration signal and the vitiated flow signal. If the observed signal is due to molecular Rayleigh scattering, the pressure throughout the flow field is both known and uniform, and the effective Rayleigh cross section is assumed

independent of composition, then the signal levels reflect total density and can be used to generate a planar temperature map of the flow field.

This approach should be valid for the vitiated air, the combusted vitiated air, and the pure hydrogen (center injector) portions of this flow field. Results are presented only for the vitiated air.

Laser-Induced Fluorescence

Laser-induced fluorescence (LIF) is a process where a laser induces a molecule to absorb light, then the molecule undergoes spontaneous emission, usually from an excited electronic state manifold. In general, the emission frequency is different from the absorption frequency. In this LIF experiment, the signal from the OH molecule expressed as the number of photoelectrons per laser pulse at a point in the laser sheet (ref. 23) is given by

$$S = N\frac{\Delta n}{n}\frac{\sigma_o}{\Delta\nu_{\text{eff}}}\Phi V\eta_{\text{eff}}\frac{\Omega}{4\pi}\eta_t\eta_{\text{PMT}} \qquad (6)$$

where N is the OH number density, $\Delta n/n$ is the fractional population in the rotational level from which excitation originates, σ_o is the integrated absorption cross section, $\Delta\nu_{\text{eff}}$ is the effective absorption line width for the transition which is computed by convolving the laser line width with the homogeneous and inhomogeneous (Doppler) line width, and η_{eff} is the fraction of excited molecules which emits a photon (the fluorescence quantum yield).

The vitiated air portion of this flow field contained O_2, N_2, and H_2O under the conditions listed in table II. These conditions will result in an OH concentration of approximately 5.5×10^{13} molecules/cm^3 if the OH were in thermodynamic equilibrium. This value was calculated using the PACKAGE chemical equilibrium code.[1] In this study, PLIF was induced by tuning the laser to the Q1(3) transition of OH. (Q1(3) as used here represents spectroscopic notation.)

Experiment

Excimer Laser Configuration

Figure 1 shows a schematic diagram of the setup for both the Rayleigh and LIF experiments. A pulsed, dual-cavity XeCl tunable excimer laser operating near 308 nm was used to probe the flow field. The laser had a pulse duration of 20 nsec, an output of 96 mJ per pulse, and a repetition rate of 10 pulses per second. The narrow-band output (0.32 cm^{-1} at FWHM) of this laser was polarized by a grating (rear reflector in the laser) and other optics in the oscillator cavity. According to the manufacturer's specifications, the output of the amplifier is approximately 20 percent s-polarized and 80 percent p-polarized. This polarization was maintained throughout the beam-shaping optics. The plane of incidence contained the laser beam and a line normal to the direction of the flow field and directed toward the camera (i.e., the X-Z plane in fig. 1). By this definition, the s-polarization was parallel to the flow field in the X direction.

The tunable excimer laser operated on the injection-locking principle. The oscillator cavity produced a low-energy spectrally narrow-bandwidth laser pulse. The pulse was injected into the amplifier. This design leads to the concept of locking efficiency, defined as the ratio of energy in a desired narrow bandwidth of radiation to the total laser energy at all frequencies produced by the laser. In this experiment, high locking efficiency was required to minimize excitation of all transitions under the laser gain profile, except for the chosen one. To improve locking efficiency, the laser was modified according to the method of Wodtke et al. (See ref. 24.) This technique was expected to increase the locking efficiency from the manufacturer's specification of 90 percent to approximately 99 percent.

Laser performance was monitored to assure the integrity of the experimental results. Changes in the following laser characteristics were also monitored: total laser energy, locking efficiency, and laser frequency. To this end, the fraction (0.1 percent) of laser light transmitted through the first beam splitter (BS1) in figure 1 was reduced in size by a factor of 10 using lenses L1 and L2. The beam was reflected by beam splitter 2 (BS2) onto a sample-and-hold photodiode detector (PD1) that monitored the total laser energy. The remaining beam was passed through the premixed hydrogen/air flat flame burner. The laser was tuned to the Q1(3) transition of OH. The resulting fluorescence was collected and imaged onto PMT1. An interference filter was used to block unwanted flame luminescence and room light. The signal from PMT1 was sampled by means of a boxcar integrator, the output of which was recorded for each laser pulse. Any decrease in the locking efficiency resulted in a signal level decrease. A block in the oscillator input produced the minimum locking efficiency and reduced the signal levels to approximately 5 percent of the peak value. This signal was also used to

[1]The PACKAGE code was developed by Aerodyne Research, Inc., Billerica, Massachusetts. Information obtained from A. Paboojian or K. Annen.

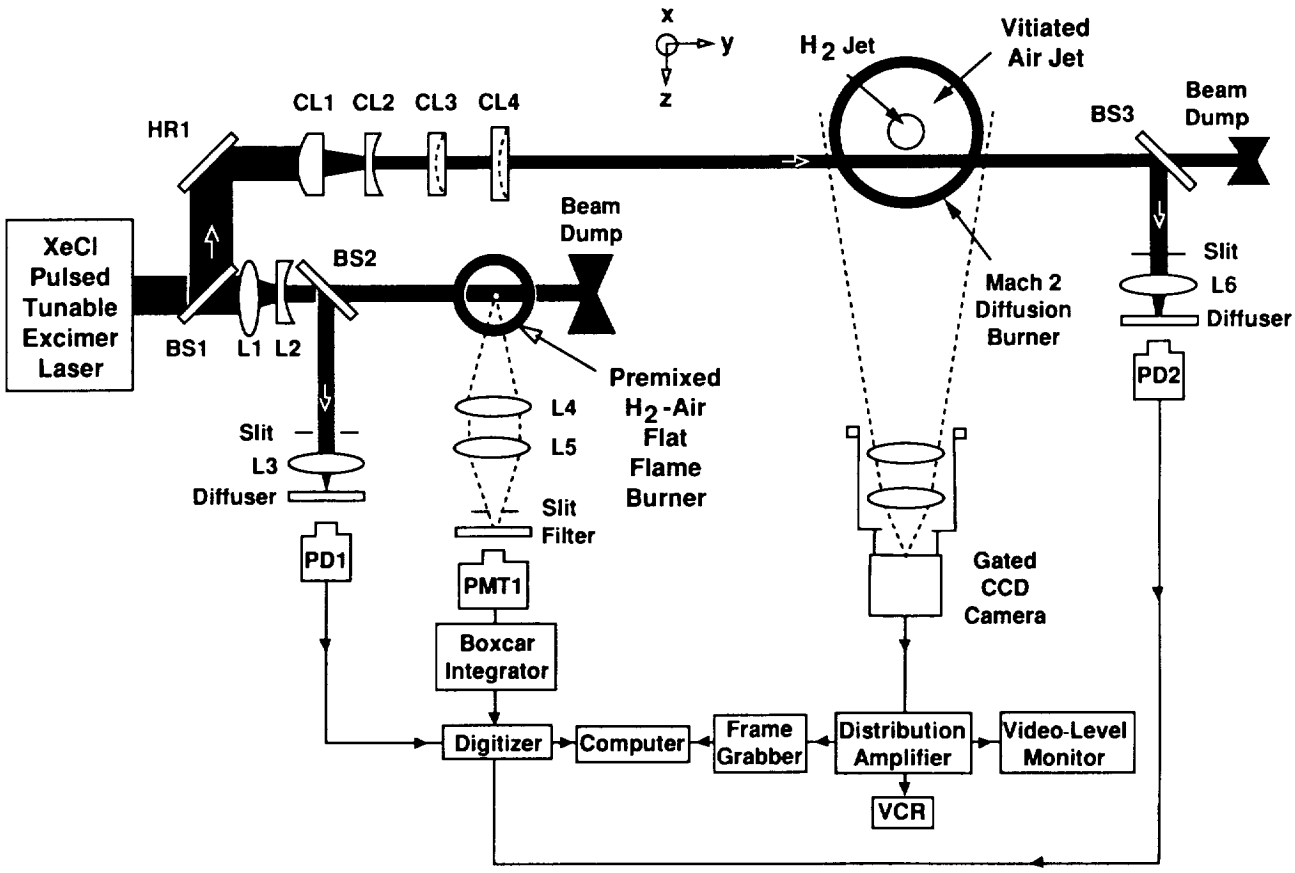

Figure 1. PRS and PLIF experimental setup. Coordinate system shown has origin on center tip of hydrogen injector.

test for long-term laser drift from the OH transition line center.

The total laser energy was monitored at two points with PD1 and PD2: PD1 was positioned before the flat flame burner; PD2 was set up to monitor the laser energy after the beam had passed through the supersonic burner. No large optics were available to image the entire large laser sheet onto the PD2 after the beam had passed through the supersonic burner. Therefore, only a small section was split off and directed onto the second photodiode. All signals were digitized and stored in a computer.

A low-resolution excitation scan (solid line in fig. 2) was taken over the gain profile of the XeCl excimer laser. The dotted line represents the laser-locking efficiency profile for this region. Signal levels were the averages of 10 laser pulses at each frequency interval. The frequency was varied by the rotation of a grating in the excimer laser. Data were acquired with the hydrogen/air flat flame burner and detection system shown in figure 1. This scan related grating position to laser frequency, which allowed the grating to be tuned to the

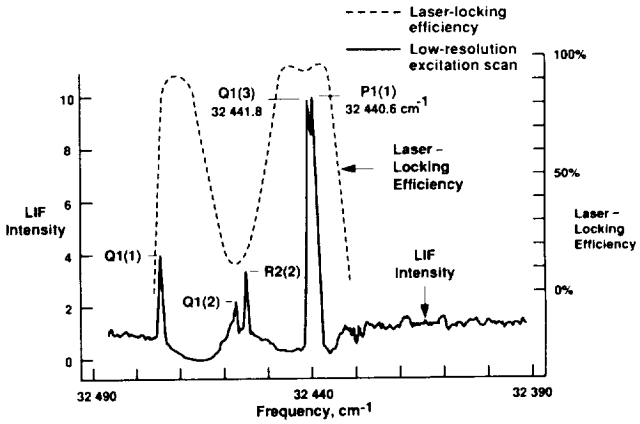

Figure 2. Low-resolution excitation scan of OH observed in hydrogen/air flat flame burner with tunable XeCl excimer laser. Locking efficiency was maximum near peak of laser profile. LIF signal levels at frequencies outside gain profile are from broadband spectral laser output that excites all OH transitions in excimer gain profile. Scan was average of 10 laser pulses at each grating step, which corresponds to 0.37 cm^{-1}. Laser tuned to 32 441.8 cm^{-1} (Q1(3) transition) to generate PLIF and to 32 465 cm^{-1} to generate PRS signals.

appropriate frequency for either PLIF or PRS data. The grating step size was approximately 0.37 cm^{-1} and the OH transition line width was approximately 0.35 cm^{-1} at FWHM in the flat flame burner. This large step size created a condition where a step was possible from one side of a transition line shape to the other without our having to sample the peak value. This step explains the observed intensity ratio Q1(3)/P1(1) $\approx$ 1 versus the calculated intensity ratio expected in the flat flame burner ($\approx$2). For the planar experiments, the resolution of the grating driver was improved by an order of magnitude. To generate PLIF, the laser was tuned to 32 441.85 cm^{-1}, which excited the Q1(3) transition in the (0-0) band of the $A\,^2\Sigma^+ \leftarrow X\,^2\pi$ system of OH. This frequency was chosen for two reasons. First, the laser-locking efficiency at this frequency was high. Second, this frequency overlapped the OH transition with a Boltzmann fraction that has less temperature dependence than any OH transition in the XeCl gain profile. The planar Rayleigh signal was generated when the laser was tuned to 32 465 cm^{-1}; this frequency was chosen because it generated the highest laser-locking efficiency and least interfered with the OH LIF.

Optical Configuration

Two cylindrical telescopes were used to form the narrow-band laser output into a sheet 6 cm high and 300 μm thick. (Beam transfer optics, BS1 and the high reflector HR1, were used to direct the laser into the telescopes.) The telescope lenses (CL1–CL4 in fig. 1) were uncoated and consisted of the following diameters and focal lengths: 50.8 $\times$ 254 mm, 50.8 $\times$ $-$63.5 mm, 50.8 $\times$ $-$203.2 mm, and 76.2 $\times$ 457 mm. The laser sheet passed through the flow and the resulting unfiltered LIF and Rayleigh signals were imaged at 90° with respect to the laser beam by the gated, double-intensified, frame transfer, charge-coupled device (CCD) in figure 1. The CCD consisted of a two-dimensional array (244 rows $\times$ 780 columns) with pixel dimensions 27 $\times$ 11.5 μm, respectively. Each of the 244 rows was divided electronically to produce the required video signal (RS-170 format), which creates actual dimensions in this same direction of approximately 14 μm. To optimize resolution along the direction of flow, the camera was rotated 90°. The intensifier gate duration was set to 300 nsec to block both room light and flame luminescence. Different planar locations in the flow field were probed by translation of the supersonic burner. All optical components remained fixed. The video signal from the camera was fed into a distribution amplifier, then was diverted to one of four output devices: the loop-through output signal was sent to a frame grabber and digitized, the second output signal was sent to a video cassette recorder, the third output signal was sent to a video-level monitoring device to determine if the detection electronics were being saturated, and the fourth output signal (not shown for clarity) was used to trigger a circuit which controlled and synchronized all the equipment required for data acquisition. The data acquisition equipment included the excimer laser, camera gate, frame grabber, and digitizer.

In the planar Rayleigh experiment, the solid angle of collection was maximized to obtain high signal levels. This maximization was accomplished by two 50.8-mm-diameter lenses with focal lengths of 152 and 76 mm that were placed 500 mm from the plane of observation. The measured resolution was approximately 1 mm parallel to the flow and 2 mm perpendicular to the flow. The demagnification was approximately 7.8x.

Calibration Procedures

The laser/camera system was calibrated to minimize uncertainties associated with the photon flux, interaction volume, solid angle of collection, optics transmission, and the differences in quantum efficiency and gain of different pixels on the CCD. Linear calibrations were assumed and based on two calibration points. The first point was obtained by measuring the Rayleigh signal generated from room air and the second obtained with the camera shutter closed. In both cases, 22 images were averaged after being normalized by the instantaneous total laser energy recorded on PD1. In this experiment, 22 images filled the available memory in the data acquisition system. For each pixel of the array, the data were used to generate a linear plot of Rayleigh signal as a function of pressure in which zero pressure was assumed when the shutter was closed. Then, a calibration file was created with a slope and intercept that corresponded to each pixel. The calibration file related signal level to pressure in torr at room temperature. This calibration was applied to the PRS signal levels obtained in the vitiated air. The result was an image with units of pressure in torr at room temperature. These units are referred to as *deduced pressure.*

A similar procedure was used for the PLIF images. However, in the PLIF results, the Rayleigh signal obtained in the calibration file was used in the calibration procedure instead of a signal resulting from the OH PLIF. Therefore, the results were expressed in terms of an arbitrary signal level. Because the signal levels generated in the PLIF experiments were high relative to the Rayleigh calibration, the camera gain was reduced by a factor of 3.2 and the

incident laser energy by a factor of 6.2 to prevent detection system saturation. This reduction was accomplished by the insertion of filters in the beam path. Measurements indicated that these actions introduced less than a 10-percent change in the relative signal levels observed by the CCD array.

The experimental data were then compared with the results of point measurements (refs. 17–20) performed on the supersonic burner. However, first the pixel position had to relate to the flow-field position. Therefore, a target was constructed that contained a matrix of squares 12 mm along each side. The target was centered on and in contact with the center injector, the camera was aligned to the target centerline, the target was illuminated by scattered 308-nm radiation, and the average of 22 images was obtained. From this average the required scale factors were obtained.

Supersonic Burner

The measurements were performed in a supersonic burner shown in figure 3 and described in references 17 and 18. The flow facility consisted of an inner central jet with an inside diameter of 2.36 mm, which injects hydrogen at a Mach number of 1, and an outer coflowing annular jet (inside diameter of 17.8 mm), which provides heated vitiated air at a Mach number of 2. The coflowing airstream at Mach 2 was heated by hydrogen combustion in the settling chamber. Then O_2 was added to replace that consumed in combustion. The resulting vitiated hot air had an oxygen content of 21 percent. The hydrogen at Mach 1 was heated indirectly; that is, the injector tube was heated by the hot, vitiated airstream. Detailed flow conditions are listed in table I. This combination of not only fuel temperature and pressure but also vitiated air temperature and pressure caused autoignition and produced a turbulent diffusion flame at the supersonic hydrogen/vitiated air interface. In this study, the vitiated air away from the flame front was studied. No measurements in the flame front are reported.

The flow rates of gases into the settling chamber as well as the center hydrogen injector were computer controlled and corrected every 6 sec to a preset value. Exit conditions in table I were calculated based on the total pressure in the settling chamber and the ratio of the area between the nozzle and the settling chamber (assuming an adiabatic expansion). A pressure tap in the wall of the settling chamber was used to monitor the total pressure continuously in the settling chamber. These measurements never varied by more than ±2 percent during a run. The burner was designed and gas parameters selected to exhaust

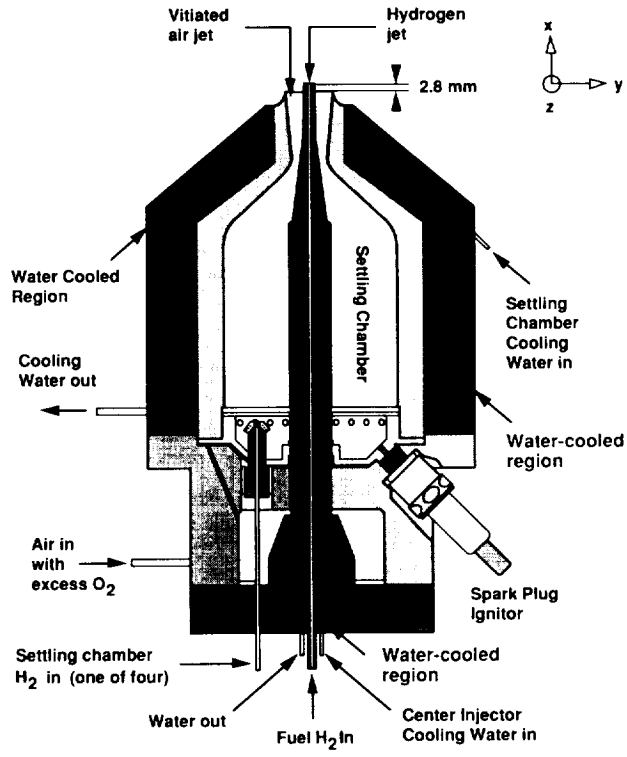

Figure 3. Supersonic burner. One of four symmetric hydrogen injectors in settling chamber shown for clarity.

into the ambient environment at a static pressure equal to atmospheric pressure.

Two other flow-field characteristics can affect the total pressure: shock waves and the turbulent shear layers (hydrogen/vitiated air interface and vitiated air/room air interface). The matched static pressure between the hot vitiated airstream and the fuel means shock waves in the flow field will be weak. No data were acquired near the hydrogen/vitiated air interface. The PRS signals near the vitiated air/room air interface show no evidence of a large pressure rise. Based on these arguments and those of the previous paragraph, the static pressure in the vitiated air portion of this flow field was assumed to vary less than 10 percent from 760 torr. This conclusion was supported by the results in references 17–20.

Results and Discussion

To facilitate comparison between these data and data obtained by other researchers, a coordinate system was defined. The center tip of the fuel injector was chosen as the origin. The tip of the center injector was approximately 2.8 mm above the top of the outer injector. The X-axis was parallel to the flow, the Y-axis was parallel to the laser sheet, and the positive Z-axis ran from the fuel injector toward

the camera. This setup is shown schematically in figures 1 and 3. The spark plug in figure 3 was used to initiate combustion in the settling chamber. After this event, the supersonic burner was translated to allow the flow field to be probed along the positive Z-axis.

Unfortunately, the location of the center fuel injector changed after the supersonic burner was ignited. Later measurements showed that it moved 0.2 to 0.4 cm along the negative Z-axis (i.e., away from the camera). In the present experiments the location of the injector position was not measured directly. Instead, a correction was made to the Z-axis coordinates that assumed an error of -0.3 cm. This correction introduced an expected uncertainty in the absolute Z-axis position of ± 0.1 cm.

Both PRS and PLIF were used to study this flow field at six locations (0.3, .4, .5, .6, .10, and .13 cm) along the Z-axis. For clarity, only the PRS and PLIF data at $Z = 0.4$ and .6 cm are presented. The latter are representative of the data obtained at all other locations. Access to all data not presented in this report can be gained by contacting the author.

Rayleigh Scattering

Figures 4(a) and 4(b) show sequential planar Rayleigh images acquired at 0.6 cm along the Z-axis. Figure 5 shows similar images acquired at $Z = 0.4$ cm. The high flow velocity (1417 m/sec in table I) and short pulse duration of the laser relative to the flow-field velocity indicate that the data represent "frozen" images of the flow. Because the interval between images was 100 msec and the flow velocity was 1417 m/sec, all images should be viewed as temporally uncorrelated. Calibration adjustments were applied and the resulting signal levels are now expressed in terms of deduced pressure at room temperature. In these experiments, the calibration was based on the effective Rayleigh cross section for room air. However, application of this curve to the experimental data will yield deduced pressures within the flow field which are too low by a factor of 1.07. The images in figures 4 and 5 are not corrected for this factor.

Figure 4(c) shows the average of 22 consecutive PRS images. (It includes the data in figs. 4(a) and 4(b).) Based on the operating conditions of the supersonic burner, deduced pressures from molecular Rayleigh signal levels inside the flow field should not exceed 760 torr. This restriction is also true for the room air outside the flow field. Consider the average image in figure 4(c). Choose a square region outside the flow field with one corner at $X = 2$ cm and $Y = 2$ cm and the lower diagonal corner at $X = 1$ cm and $Y = 2.5$ cm. This region was chosen because it was farthest from the flow field and signal levels should be due only to room air constituents. The resulting mean and standard deviation (σ) of the deduced pressure in this region based on statistical averages are 741 ± 46 torr and 2σ, respectively. These signal levels were consistent with molecular Rayleigh

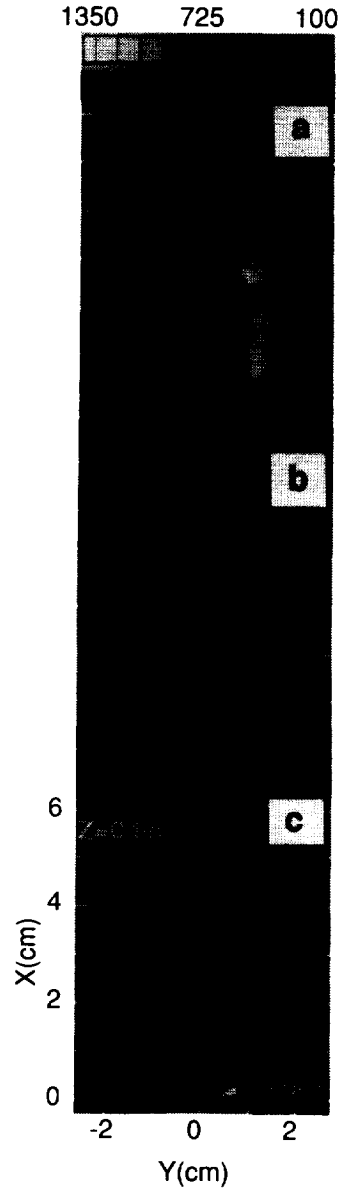

Figure 4. Planar Rayleigh images at $Z = 0.6$ cm. Gray scale is in torr. Parts (a) and (b) show instantaneous Rayleigh images converted to deduced pressure at room temperature. Data were normalized for camera gain change of a factor of 2.4. Part (c) shows average Rayleigh image based on sum of 22 images.

scattering and none higher were expected in these images. However, the signal levels in certain regions of figures 4(a) and 6 exceeded this value. Any signal levels in the Rayleigh images which exceeded the maximum expected statistical average by more than 4σ are now referred to as anomalous. (The anomalous signals are discussed later.)

Previously we have shown that if the observed Rayleigh signal was due mainly to molecular Rayleigh scattering, the pressure throughout the flow field was assumed uniform and equal to 760 torr, and the effective Rayleigh cross section was independent of composition, then the signal levels reflect density and can be used to generate a planar temperature map of the flow field. To demonstrate the latter, the average data in figure 4(c) have been converted to temperature. The resulting image is presented in figure 6(a). A line taken across figure 6(a) at $X = 2$ cm shows the temperature variation shown in figure 6(b). At $Y = 0$ cm in figure 6(b), this temperature was 1000 ± 200 K (2σ). This uncertainty was based on fluctuations in the Rayleigh-derived temperature observed at $X = 2.5 \pm 0.5$ cm along the image centerline. The data were acquired at 0.6 ± 0.1 cm along the Z-axis. The expected temperature based on the experimental data in reference 20 is 1250 ± 220 K (2σ). This level of agreement demonstrates the potential for using Rayleigh scattering to obtain planar temperature maps of the vitiated air component of this and similar flow fields.

The instantaneous PRS data in figures 4 ($Z = 0.6$ cm) and 5 ($Z = 0.4$ cm) illustrate several results. First, the PRS data were acquired with the camera gain reduced by a factor of 2.4 with respect to the calibration data to minimize saturation of the detection system from anomalous signals. All images were corrected accordingly. The average signal levels outside the flow corresponded within ± 10 percent to 760 torr, which indicated that the camera gain reduction was accounted for quantitatively. Second, the PRS signal levels provided a method of identifying the approximate location of the boundary between the vitiated air flow and room air. Third, signal levels decreased from the vitiated air/room air interface to the centerline of the image. This change was as expected for a technique which measures total number density and hence temperature. Fourth, for the 22 images used to generate figure 4(c), the statistical standard deviation at most locations in the flow field was < 10 percent (1σ). For reference, the statistical variation observed in the calibration data was <4 percent. This variation compares well with the measurements in references 19 and 20 in which root mean square (rms) fluctuations of ≈ 10 percent were observed in the temperature and the mole fractions of nitrogen, oxygen, and water near these locations.

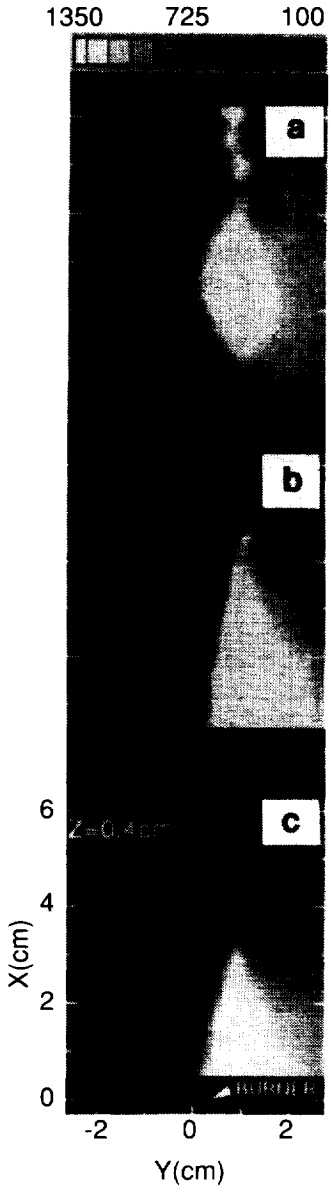

Figure 5. Planar Rayleigh images at $Z = 0.4$ cm. Gray scale is in torr. Parts (a) and (b) show instantaneous Rayleigh images converted to deduced pressure at room temperature. Data were normalized for camera gain change of a factor of 2.4. Large signal level changes in images required change in gray scale to 100–1350 torr for comparison with other figures. Signal levels rise far above this level. In part (b), signals near $Y = 1$ cm and $X = 2 \pm 1$ cm range from 1350 to 3000 torr. Above 3000 torr, detector saturated. Part (c) shows average Rayleigh image based on sum of 22 images.

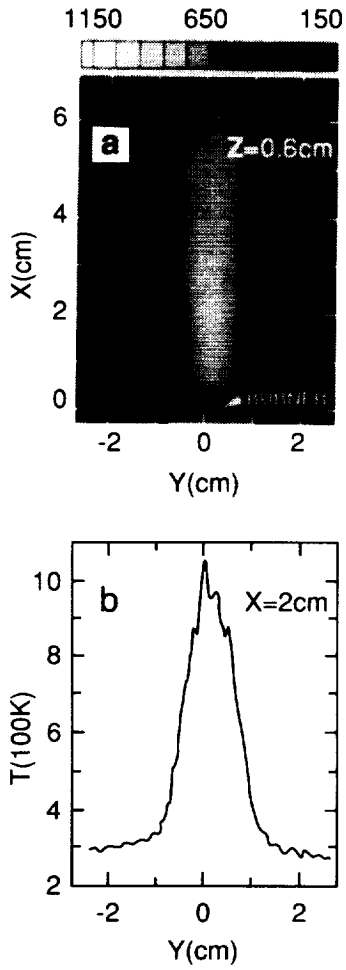

Figure 6. Temperature image based on average Rayleigh data at $Z = 0.6$ cm. Temperature gray scale is in Kelvin. Part (a) shows data taken from figure 4(c). Part (b) shows single row of data from figure 6(a) at $X = 2$ cm.

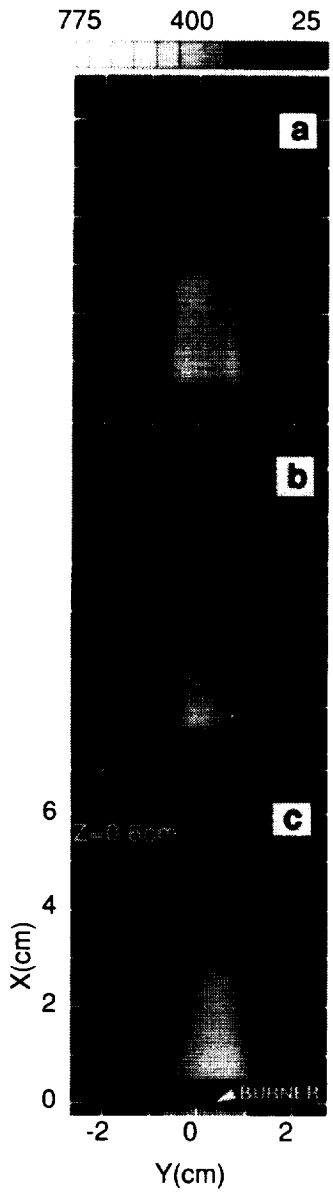

Figure 7. Instantaneous PLIF images at $Z = 0.6$ cm. Gray scale represents relative signal levels. Images in parts (a) and (b) were not normalized for changes in camera gain or laser attenuation (corresponding to factor of ≈ 20 relative to data in fig. 4). Part (c) shows average PLIF image based on sum of 22 images.

Planar Laser-Induced Fluorescence

Data based on OH were acquired at the same locations as the Rayleigh data and are presented in figures 7 and 8. The high PLIF signal levels required that the laser energy be reduced by a factor of 6.2 and the camera gain by a factor of 3.2 with respect to the Rayleigh calibration data. These two reductions minimized saturation in the detection system when OH images were acquired. A comparison of the data of figures 4 and 5 with the data of figures 7 and 8 shows that near the image centerline, the contribution of molecular Rayleigh scattering signal to the total signal levels in the PLIF images is less than 5 percent.

In a gaseous environment in which OH is at equilibrium, the OH concentration will increase as the temperature increases. Based on the Rayleigh results in this study and results in references 19 and 20, the temperature increases from room air toward the supersonic burner centerline. If the OH is in equilibrium, then PLIF signal levels should increase from the room air interface to the supersonic burner centerline. This general trend is evident in the average images in figures 7 and 8 and proves that the signals were due primarly to OH. The signal level trends observed in the PLIF data were the opposite of trends observed in the Rayleigh data.

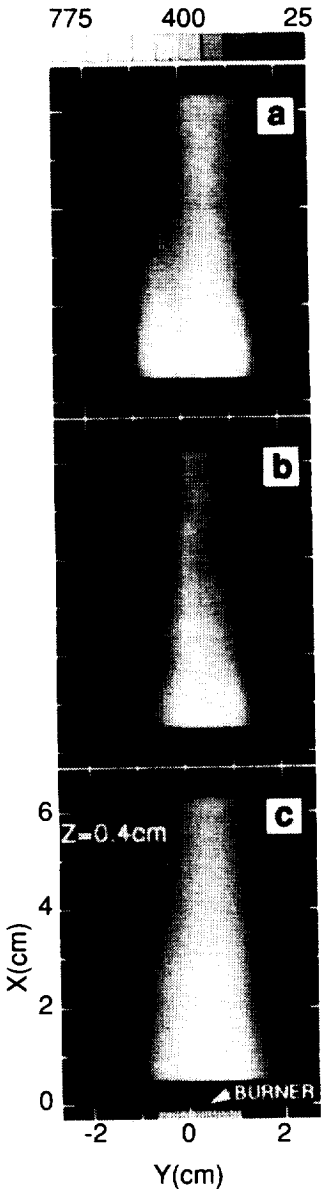

Figure 8. Instantaneous PLIF images at $Z = 0.4$ cm. Gray scale represents relative signal levels. Images in parts (a) and (b) are similar to those in figure 7. Part (c) shows average PLIF image based on sum of 22 images.

Consider the PLIF data in figures 7 and 8. The instantaneous PLIF images showed that the spatial and temporal OH signal profiles in the vitiated airstream were not uniform as portrayed in the average images. The instantaneous images showed striation patterns or alternating regions of high and low signal levels along the Y-axis. They also showed that the locations and widths of these patterns vary from image to image. Along the Y-axis, the relative OH signal levels varied by as much as a factor of 2. The signal levels observed in the PLIF images can be generated from three sources: LIF from OH, molecular Rayleigh scattering, and anomalous signals. As discussed earlier, molecular Rayleigh scattering contributes less than 5 percent to the total signal under these conditions. The striation patterns were observed at many locations along the Y-axis, so they cannot be the result of anomalous Rayleigh signals localized along the vitiated air/room air interface. Therefore, they must be due to LIF from OH.

To investigate these observations further, the experimental setup was modified. Using a single 203-mm cylindrical lens, we focused the beam into a sheet that is 25 mm high by 0.08 mm thick. An ultraviolet lens (105 mm, f/4.5) was used to collect and focus the PLIF signal onto the camera. This setup resulted in a resolution of approximately 0.025 cm along the X-axis and 0.035 cm along the Y-axis. Three of the 22 images acquired with this experimental setup at a location of 0.6 cm are presented in figure 9. These images show both the striation patterns in the flow field and the eddy patterns inherent in the vitiated air. In figure 9, OH signal levels along the Y-axis can vary by as much as a factor of 3. All the PLIF images observed in the flow field showed these striations to some degree. The differences in sheet thickness in figure 9 (0.08 cm) and figures 7 and 8 (0.30 cm) and the resulting observations indicate that this striation was a spatially localized phenomenon.

To determine the cause of the striation patterns, the parameters in equation (6) which could affect signal levels were examined. These include the transition line width, $\Delta n/n$ (the Boltzmann fraction), the fluorescence quantum yield, and the OH density. All were functions of temperature. Based on the PRS data along with the data in references 19 and 20, the maximum instantaneous absolute temperature variation across the center 66 percent of the vitiated air flow field was 800 to 1500 K. The striation patterns cannot be due to changes in the transition line shape. In vitiated air at 1250 K, the line shape can be described by a Voigt profile. The inhomogeneous or Doppler broadening was approximately 0.20 cm^{-1} and the homogeneous broadening was approximately 0.06 cm^{-1}. This broadening resulted in a transition line width of approximately 0.23 cm^{-1}. The manufacturer's specified laser line width was 0.32 cm^{-1}. Because the Voigt profile was dominated by Doppler broadening, it was essentially independent of composition and depended on the square root of temperature. From 800 to 1500 K, the Voigt profile changed <25 percent and the convolution of the Voigt profile with the laser profile changed <10 percent. The

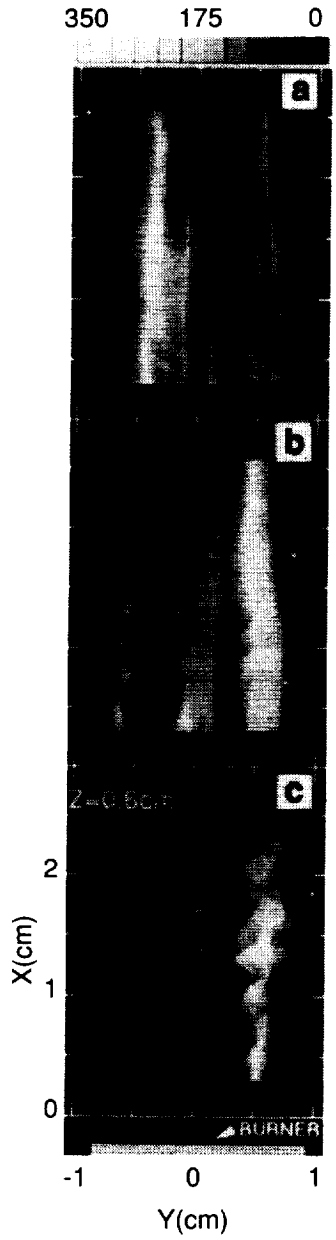

Figure 9. Instantaneous PLIF images acquired at high resolution and at $Z = 0.6$ cm. Gray scale represents relative signal level.

striation patterns may have been due to changes in the Boltzmann fraction because it changed by 70 percent from 800 to 1500 K for this transition. However, if the temperatures in the instantaneous flow field varied greatly, they should have been observed in the PRS images. Even though the sheet thickness in the PRS was 300 μm, no evidence of striation patterns were observed.

In this flow field, water dominated the quenching process. Little information can be found in the literature on the temperature-dependent quenching cross sections for water. However, based on what data are available, the quenching cross section varies less than 20 percent from 800 to 1500 K. Water concentration changes of 100 to 200 percent could create the observed signal changes by influencing quenching. However, the authors of references 19 and 20 have measured rms fluctuations in this region for major species densities (N_2, O_2, and H_2O) of approximately 10 percent. The striation patterns were probably not the result of water nonuniformities. Finally, OH density changes of 100 to 200 percent could explain the striation patterns. If the OH were in thermodynamic equilibrium, the density would vary as a function of temperature. For a temperature change of 1200 to 1300 K, the equilibrium OH concentration varies by a factor of 3.5. (See footnote 2.) This temperature variation is well within the uncertainties in the Rayleigh results as well as those in references 19 and 20. Thus, based on the available information, the observed striation patterns are most likely the result of small localized instantaneous temperature nonuniformities in the vitiated air.

Although the cause of these temperature nonuniformities is not fully understood, a distinct possibility may be the design and location of the hydrogen injectors in the settling chamber. These injectors are approximately transverse to the air flow. (See refs. 17 and 18.) The instantaneous mixing of fuel and air in the settling chamber around the hydrogen injectors may not have been uniform. This nonuniformity could result in instantaneous localized regions of varying hydrogen concentration. The resulting oxidation of hydrogen could produce the observed striation patterns. Therefore, the injector design in conjunction with incomplete mixing is likely both the cause of the eddy patterns as well as the reason they can be observed in figure 9.

Anomalous Signals

The application of planar Rayleigh scattering to this flow field has shown anomalously high signal levels near the vitiated air/room air interface. These high levels can be seen in figures 4(a) and 5. None were observed in the instantaneous images beyond 0.6 cm along the Z-axis. In all individual images probed at 0.3 to 0.6 cm along the Z-axis, these anomalous flow features were observed only on the right side of the images near the vitiated air/room air interface. From the outer edge of the Mach 2 flow

[2] PACKAGE code obtained from A. Paboojian or K. Annen, Aerodyne Research, Inc., Billerica, Massachusetts.

field along the Z-axis toward the origin, the spatial and temporal frequencies, intensities, and lengths of these features increased. This change can be seen in figures 4 and 5. These features were observed in 2 of the 22 images acquired at $Z = 6$ cm and in 21 of the 22 images at $Z = 4$ cm. Two anomalous images did not affect the average image shown in figure 4(c), but 21 of the 22 images dominated the final average shown in figure 5(c). At both locations, the camera gain was decreased by a factor of 2.4 relative to the calibration data. All Rayleigh data presented were corrected for this factor. No images at the location of figure 4 show saturation, but 11 of the 22 images which contribute to figure 5(c) exhibit localized saturation.

Consider a given spatial location in two sequential images which was first unaffected then affected by the anomalous signals. Instantaneous and average PRS deduced pressures without these flow features range from 350 to 600 torr; the deduced pressures generated by these anomalous flow features range from 1000 to 3000 torr. Above 3000 torr the detection system saturated. This flow exhausted into the atmosphere at a matched static pressure. (See table I.) This fact, the confirmed (refs. 17–20) mole fraction data in table II, the Rayleigh cross sections in table III, and the flow-field signal levels without these anomalous flow features indicate that no molecular gaseous species in this flow field with a product of density and Rayleigh cross section was large enough to generate the signal levels. Therefore, the signal levels could not have been generated by molecular Rayleigh scattering from a gaseous species.

The locking efficiency of the tunable excimer laser was not 100 percent. Some researchers might argue that the anomalous signals in figures 4 and 5 perhaps could have been localized pockets of OH in high concentration that were excited by the unlocked laser fraction. However, the laser was predicted to be approximately 1 percent unlocked and approximately 5 percent of the unlocked portion of the laser overlaps OH transitions. If the anomalous signals were due to pockets of OH, similar pockets should have been observed in the PLIF images; however, the PLIF images showed no such pockets. Therefore, the anomalous signal levels in the Rayleigh images cannot be due to localized pockets of OH in high concentration that were excited by the unlocked laser fraction.

This problem can also be viewed as follows. Assume that the anomalous PRS signals were due to OH. The data indicate that these signal levels decreased by more than a factor of 2 over 2.5 cm of the flow field after being ejected from the supersonic burner. This level corresponds to approximately 20 μsec. In this flow, OH can be removed by reaction with O, H_2, and OH with the following Arrhenius expressions from reference 25 in cm^3/molecule-sec: 2.99×10^{-11}, $1.7 \times 10^{-16} T^{1.6} \exp(-13.8 \text{ kJ}/RT)$, and $1 \times 10^{-11} \exp(-4.6 \text{ kJ}/RT)$. The equilibrium O-atom concentration was 1.8×10^{11} molecules/cm^3. References 19 and 20 quoted average hydrogen mole fractions of less than 0.0001. Therefore, both reactions were too slow to remove OH in 20 μsec. For self-reaction to remove the OH, a concentration of 10^{16} molecules/cm^3 was required. The equilibrium OH concentration was 5.5×10^{13}. If more than two orders-of-magnitude difference existed in the localized OH concentration about the PLIF image centerline, the instantaneous and average PLIF images should have easily detected this variance; however, no such signal level changes were observed. Therefore, the anomalous signals observed in the PRS images were not the result of OH excitation by the unlocked laser fraction.

In the previous paragraphs the argument has been presented that no molecular gaseous component of this flow field can produce the observed anomalous signals. Therefore, the anomalous signals were the result of scattering from a nongaseous species. Two sources of nongaseous scattering species are possible. One possibility was metal flakes (nickel or stainless steel) that were ejected from the inner walls of the settling chamber. This flaking was unlikely because the large quantity of material ejected should have rapidly disintegrated the supersonic burner. Also, as the height above the surface of the supersonic burner increased, the spatial and temporal frequency, intensity, and length of the features decreased until they were no longer observed. Few features were observed above $X = 10$ cm and none were observed above 15 cm. Metallic flakes should not vaporize at the temperatures near the vitiated air/room air interface.

The other possibility was liquid water. Although unlikely in a combustion environment, the presence of liquid water could explain several observations. The first observation was the elongated size of the anomalous flow features, which would be the expected shape for liquid water detaching from a surface. Second, the liquid water would vaporize as it traveled downstream. Finally, the presence of liquid water could explain the temperature, OH, and water asymmetries observed by other researchers (refs. 17–20) in the supersonic burner. The vitiated air flow was 25-percent water after complete combustion in the settling chamber.

The settling chamber has water-cooled walls. Gaseous water could conceivably condense on the

settling chamber walls, be channeled to a localized region, and be ejected along the edge of the outer injector. If this hypothesis is correct, an increase in the temperature of the settling chamber walls should lower the anomalous signal levels. We can alter the temperature by varying the flow rate of the water that cools the settling chamber. Subsequent tests based on this analysis were performed by another researcher. (Personal communication with G. Diskin, Langley Research Center, Hampton, Virginia.) As the settling chamber wall temperature increased, the anomalous signal levels decreased. Also, the center injector and settling chamber walls were cooled with separate water supply controls. Variances in the water flow caused observable anomalous signals from either the center or the outer injector. This experiment supports the hypothesis that liquid water was being injected into the flow field.

Conclusions

The use of planar Rayleigh scattering (PRS) and planar laser-induced fluorescence (PLIF) to investigate the vitiated air component of a coaxial hydrogen/vitiated air nonpremixed turbulent jet flame at a Mach number of 2 has produced several results.

1. The signal is sufficient to obtain planar information in the vitiated air component of an unseeded, hot, annular jet at a Mach number of 2 and at atmospheric pressure by using both PRS and PLIF. Both techniques can be implemented using a single xenon chloride tunable excimer laser.

2. The PRS technique produced a signal that can be converted into a temperature map. This conversion is possible because the pressure of the flow field was assumed known and uniform and because calculations here have shown that the major components in the flow field had an effective Rayleigh cross section that can be considered independent of composition. The measured temperatures in this study agreed well with those obtained by previous researchers and with the values based on the adiabatic and isentropic expansion. The PRS data also indicated that fluctuations in both temperature and density are minimal (<10 percent) for a large area of the vitiated air portion of this flow field. This finding also agrees with results published by previous researchers.

3. The use of PLIF to obtain qualitative information has revealed the following: First, the hydroxyl molecule was ejected from the settling chamber with the vitiated air in sufficient concentration to generate planar images of the flow field. Second, the PLIF images showed evidence of striation patterns; these are most likely the result of small localized instantaneous temperature nonuniformities in the vitiated air. The cause of these nonuniformities is not fully understood; the hydrogen injector design, location, or orientation in the settling chamber may cause them. Third, the PLIF data reveal evidence of eddy patterns in the vitiated air. Both the striation and eddy patterns show that some components of the vitiated air flow field were unsteady. This unsteadiness is expected to propagate into the fuel/vitiated air region and may create or enhance fluctuations in the reacting part of this flow. Any attempt to understand the combustion process in a supersonic nonpremixed jet flame must include a detailed understanding of the properties of the vitiated air flow.

4. The results from both the PLIF and PRS techniques have revealed that a nongaseous flow component is localized near the vitiated air/room air interface. The arguments and experimental observations suggest that this component was the result of liquid water that condensed on the walls of the settling chamber and subsequently was ejected into the flow field. This condensation problem is possible in similarly designed supersonic burners and must be minimized before meaningful measurements can be obtained.

NASA Langley Research Center
Hampton, VA 23681-0001
July 21, 1994

References

1. Boutier, A., ed.: *New Trends in Instrumentation for Hypersonic Research.* Volume 224, Kluwer Academic Publ., 1992, pp. 1–10.

2. Monaghan, R. J.: The Use of Pitot Tubes in the Measurement of Laminar Boundary Layers in Supersonic Flow. *Papers Presented at the Seventh Meeting of the Wind Tunnel and Model Testing Panel (Ottawa)*, AGARD, June 1955, pp. 101–131. (Available from DTIC as AD 109 913.)

3. Ashby, George C., Jr.: Miniaturized Compact Water-Cooled Pitot-Pressure Probe for Flow-Field Surveys in Hypersonic Wind Tunnels. Proceedings *of the 34th International Instrumentation Symposium*, ISA, 1988, pp. 159–166. (Available as ISA Paper 88-0718.)

4. Shirinzadeh, B.; Hillard, M. E.; Balla, R. Jeffrey; Waitz, I. A.; Anders, J. B.; and Exton, R. J.: Planar Rayleigh Scattering Results in Helium-Air Mixing Experiments in a Mach-6 Wind Tunnel. *Appl. Opt.*, vol. 31, no. 30, Oct. 20, 1992, pp. 6529–6534.

5. Dibble, R. W.; and Hollenbach, R. E.: Laser Rayleigh Thermometry in Turbulent Flames. *Eighteenth Symposium (International) on Combustion*, Combust. Instu., 1981, pp. 1489–1499.

6. Fourguette, D. C.; Zurn, R. M.; and Long, M. B.: Two-Dimensional Rayleigh Thermometry in a Turbulent Nonpremixed Methane-Hydrogen Flame. *Combust. Sci. & Tech.*, vol. 44, 1986, pp. 307-317.

7. Escoda, M. Carla; and Long, Marshall B.: Rayleigh Scattering Measurements of the Gas Concentration Field in Turbulent Jets. *AIAA J.*, vol 21, no. 1, Jan. 1983, pp. 81–84.

8. Long, Marshall B.; Levin, Philip S.; and Fourguette, Dominique C.: Simultaneous Two-Dimensional Mapping of Species Concentration and Temperature in Turbulent Flames. *Opt. Let.*, vol. 10, no. 6, June 1985, pp. 267–269.

9. Miles, R.; and Lempert, W.: Two-Dimensional Measurement of Density, Velocity, and Temperature in Turbulent High-Speed Air Flows by UV Rayleigh Scattering. *Appl. Phys. B*, vol. 51, 1990, pp. 1–7.

10. Barlow, R. S.; Fourguette, D. C.; Mungal, M. G.; and Dibble, R. W.: Experiments on the Structure of an Annular Compressible Reacting Shear Layer. *AIAA J.*, vol. 30, no. 9, Sept. 1992, pp. 2244–2251.

11. Seitzman, Jerry M.; Üngüt, Aziz; Paul, Phillip H.; and Hanson, Ronald K.: Imaging and Characterization of OH Structures in a Turbulent Nonpremixed Flame. *Twenty-Third Symposium (International) on Combustion*, Combust. Instu., 1990, pp. 637–643.

12. Hanson, Ronald K.; Seitzman, Jerry M.; and Paul, Phillip H.: Planar Laser-Fluorescence Imaging of Combustion Gases. *Appl. Phys. B*, vol. 50, 1990, pp. 441–454.

13. Hanson, Ronald K.: Combustion Diagnostics: Planar Imaging Techniques. *Twenty-First Symposium (International) on Combustion*, Combust. Instu., 1986, pp. 1677–1691.

14. Becker, H.; Arnold, A.; Suntz, R.; Monkhouse, P.; Wolfrum, J.; Maly, R.; and Pfister, W.: Investigation of Flame Structure and Burning Behaviour in an IC Engine Simulator by 2D-LIF of OH Radicals. *Appl. Phys. B*, vol. 50, 1990, pp. 473–478.

15. Suntz, R.; Becker, H.; Monkhouse, P.; and Wolfrum, J.: Two-Dimensional Visualization of the Flame Front in an Internal Combustion Engine by Laser-Induced Fluorescence of OH Radicals. *Appl. Phys. B.*, vol. 47, 1988, pp. 287–293.

16. Kychakoff, George; Howe, Robert D.; and Hanson, Ronald K.: Quantitative Flow Visualization Technique for Measurements in Combustion Gases. *Appl. Opt.*, vol. 23, no. 5, Mar. 1, 1984, pp. 704–712.

17. Jarrett, Olin, Jr.; Cutler, Andrew D.; Antcliff, Richard R.; Tawit, Chitsomboon; Dancey, Clinton L.; and Wang, Jian An: Measurements of Temperature, Density, and Velocity in Supersonic Reacting Flow for CFD Code Validation. 25th JANNAF Combustion Meeting, Oct. 1988.

18. Antcliff, Richard R.; Jarrett, Olin, Jr.; Chitsomboon, Tawit; and Cutler, Andrew: CARS Measurements of Temperature and Species Number Density in Supersonic Combusting Flow. AIAA-88-4662, Sept. 1988.

19. Cheng, T. S.; Wehrmeyer, J. A.; Pitz, R. W.; Jarrett, O., Jr.; and Northam, G. B.: Finite-Rate Chemistry Effects in a Mach 2 Reacting Flow. AIAA-91-2320, June 1991.

20. Cheng, T. S.; Wehrmeyer, J. A.; and Pitz, R. W.: *Laser Raman Diagnostics in Subsonic and Supersonic Turbulent Jet Diffusion Flames.* NASA CR-189544, 1991.

21. Shardanand; and Prasad Rao, A. D.: *Absolute Rayleigh Scattering Cross Sections of Gases and Freons of Stratospheric Interest in the Visible and Ultraviolet Regions.* NASA TN D-8442, 1977.

22. Gardiner, W. C., Jr.; Hidaka, Y.; and Tanzawa, T.: Refractivity of Combustion Gases. *Comb. & Flame*, vol. 40, 1981, pp. 213–219.

23. Killinger, D. K.; Wang, Charles C.; and Hanabusa, M.: Intensity and Pressure Dependence of Resonance Fluorescence of OH Induced by a Tunable UV Laser. *Phys. Rev. A*, vol. 13, no. 6, June 1976, pp. 2145–2152.

24. Wodtke, A. M.; Hüwel, H.; Schlüter, H.; and Andresen, P.: Simple Way to Improve a Tunable Argon Fluoride Laser. *Rev. Sci. Inst.*, vol. 60, no. 4, Apr. 1989, pp. 801–802.

25. Warnatz, Jürgen: Rate Coefficients in the C/H/O System. *Combustion Chemistry*, W. C. Gardiner, Jr., ed., Springer-Verlag, 1984, pp. 197–346.

REPORT DOCUMENTATION PAGE

Form Approved
OMB No. 0704-0188

1. AGENCY USE ONLY *(Leave blank)*	2. REPORT DATE	3. REPORT TYPE AND DATES COVERED
	October 1994	Technical Memorandum

4. TITLE AND SUBTITLE
Planar Rayleigh Scattering and Laser-Induced Fluorescence for Visualization of a Hot, Mach 2 Annular Air Jet

5. FUNDING NUMBERS
WU 505-70-91-01

6. AUTHOR(S)
R. Jeffrey Balla

7. PERFORMING ORGANIZATION NAME(S) AND ADDRESS(ES)
NASA Langley Research Center
Hampton, VA 23681-0001

8. PERFORMING ORGANIZATION REPORT NUMBER
L-17374

9. SPONSORING/MONITORING AGENCY NAME(S) AND ADDRESS(ES)
National Aeronautics and Space Administration
Washington, DC 20546-0001

10. SPONSORING/MONITORING AGENCY REPORT NUMBER
NASA TM-4576

11. SUPPLEMENTARY NOTES

12a. DISTRIBUTION/AVAILABILITY STATEMENT
Unclassified–Unlimited

Subject Category 12

12b. DISTRIBUTION CODE

13. ABSTRACT *(Maximum 200 words)*

Planar Rayleigh scattering (PRS) and planar laser-induced fluorescence (PLIF) were used to investigate the vitiated air component of a coaxial hydrogen/vitiated air nonpremixed turbulent jet flame that is ejected at a Mach number of 2. All experiments were performed with a xenon chloride tunable excimer laser. Planar information for both techniques was obtained using laser sheets 6 cm high, 5 cm wide, and 300 μm thick. In this flow field, the effective Rayleigh cross section of the components in the vitiated air was assumed to be independent of composition. Therefore, the PRS technique produced signals which were proportional to total density. When the flow field was assumed to be at a known and uniform pressure, the PRS signal data for the vitiated air could be converted to temperature information. Also, PLIF images were generated by probing the OH molecule. These images contain striation patterns attributed to small localized instantaneous temperature nonuniformities. The results from the PLIF and PRS techniques were used to show that this flow field contains a nongaseous component, most likely liquid water that can be reduced by increasing the settling chamber wall temperature.

14. SUBJECT TERMS
Planar Rayleigh scattering; Supersonic combustion; Planar laser-induced fluorescence; CFD validation

15. NUMBER OF PAGES
16

16. PRICE CODE
A03

17. SECURITY CLASSIFICATION OF REPORT	18. SECURITY CLASSIFICATION OF THIS PAGE	19. SECURITY CLASSIFICATION OF ABSTRACT	20. LIMITATION OF ABSTRACT
Unclassified	Unclassified	Unclassified	